NJC

PAPER

Check for updates

In situ replacement of Cu-DEN: an approach for preparing a more noble metal nanocatalyst for catalytic use†

Oluwatayo Racheal Onisuru, Charles O. Oseghale and Reinout Meijboom ⓘD *

The advantage of dendritic monodisperse macromolecules' dual templating ability was useful in the formation of silica-supported copper nanoparticles $Cu_n@SiO_2NPs$. This was acquired by the initial synthesis of a silica framework ($G4$-PAMAM-NH_2-SiO_2) as a mesoporous support using amine-terminated generation 4 PAMAM dendrimers ($G4$-PAMAM-NH_2). The encapsulated $Cu_n@SiO_2$ NPs, calcined at 500 °C, were made to undergo a displacement reaction with Au^{3+} generated from the equivalent molar addition of $HAuCl_4$. This resulted in the formation of $Au_n@SiO_2NPs$ upon *in situ* replacement at a regulated pH. The synthesized nanoparticles were characterized and examined. The catalysts were shown to be catalytically active in the hydrogenation of 4-nitrophenol, and oxidation of rhodamine B as model reactions, before oxidation of styrene using TBHP. Also, the stability of the catalyst was evaluated, and the catalytic activity was retained after three consecutive cycles.

1. Introduction

The diverse applications of nanoparticles will continually make them the subject of focus among researchers. This is due to the uniqueness of their excellent performance in the enhancement of selectivity and productivity. Metal nanoparticles are making ways for imaginable innovations in the field of catalysis.[1] The crucial characteristics of large surface area to volume ratio possessed by metal nanoparticles has an unparalleled implication on their performance. Generally, under normal conditions, to prevent agglomeration, they are produced in the presence of stabilizers. This provides control over the particle size formed.[2] Focus had long been on the use of dendrimers as stabilizers for metal nanoparticles, which has led to extensive research being carried out over the years on the formation of dendrimer-encapsulated nanoparticles.[1–11] Dendrimers are macromolecules with a three-dimensional structure with a globular shape that can easily host metal nanoparticles for use in catalysis.[1] However, the synthetic protocols of some metal nanoparticles are not always easily and quickly achieved as anticipated. This is illustrated by dendrimer-encapsulated platinum nanoparticles (Pt-DENs), which take at least 72 hours before complete complexation between the metal ions and dendrimer can be achieved.[12] Hence, a faster alternative route is required.

The synthesis of dendrimer-encapsulated copper nanoparticles (CuDENs) stabilized by generation 4 amine-terminated PAMAM ($G4$ PAMAM-NH_2) dendrimers was carried out. An effort was also made to immobilize the colloidal CuDENs on a mesoporous silica support to form heterogeneous catalysts. Heterogeneous catalysts have the advantage of recoverability and separation from the reaction medium compared to homogeneous catalysts.[3] Silica has been in use as a mesoporous support for metal nanoparticles by researchers in the field.[13–16] It has been reported that mesoporous silica materials are not only excellent in chromatographic, cosmetic, and photographic use, but also for catalytic applications.[17] Hence, much interest has been shifted to its use. Yanqiu and coworkers[18] reported the fabrication of hollow MCM-41 (Mobil Composition of Matter No. 41) microspheres through the assemblage of tetraethyl orthosilicate (TEOS) coupled with a dual template. The dual template acquired was prepared by dissolving cetyltrimethylammonium bromide (CTAB) in poly(styrene-methyl methacrylate) microsphere soap-free latex and by consecutive removal of the polymer core present in tetrahydrofuran.[18]

In this study, we utilized the hydrolysis of TEOS together with hydrochloric acid at room temperature for the mesoporous silica sphere synthesis, which has a different phase for the immobilization of CuDENs. This is an advantageous route for preparing silica-supported gold nanoparticles ($Au_n@SiO_2$ NPs), through an *in situ* galvanic exchange with gold after an initial synthesis of $Cu_n@SiO_2$ NPs. This was followed by the addition of Au^{3+} metal atom (Au) to the presynthesized NPs as shown in Scheme 1. Au is nobler, having higher potential power

Research Centre for Synthesis and Catalysis, Department of Chemical Sciences, University of Johannesburg, P. O. Box 524, Auckland Park, Johannesburg 2006, South Africa. E-mail: rmeijboom@uj.ac.za; Fax: +27 11 559 2819; Tel: +27 72 894 0293
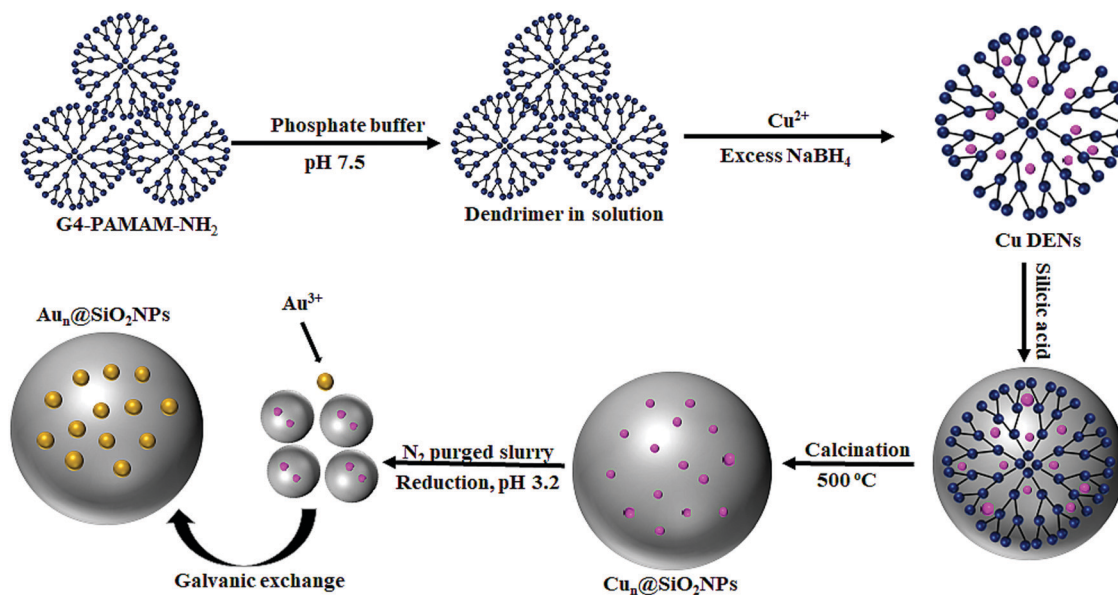
Scheme 1 Schematic illustration of CuDEN immobilization on silica and subsequent *in situ* replacement.

electrochemically and capable of simultaneous reduction as the replacement takes place.[19] Such a catalyst is likely to have a considerable impact on catalysis.

However, one drawback of Cu-based catalyst synthesis is their non-tolerance of oxygen.[20] They are quick to oxidize in the presence of air. Therefore, the synthesis was carried out under inert conditions before taking advantage of $Cu_n@SiO_2NPs$ for the replacement reaction with Au for the formation of $Au_n@SiO_2NPs$. Meanwhile, this replacement was propelled by the smaller standard electrode potential of +0.340 E° (volts) possessed by Cu^{2+}, which made the ease of exchange by Au^{3+} having 1.50 E° volts, a possibility.

Replacement reactions occur when a metal ion of higher oxidative potential meets another metal atom of smaller standard electrode potential. This results in the dissolution of the surface metal atom by oxidation and consequent reduction of the metal ion with higher oxidative potential.[19] Hence, galvanic replacement is the displacement that takes place when there is a replacement of one zero-valent metal by another more noble metal to produce stable, well-dispersed, and compositionally pure metal atom nanoparticles made by a reduced precursor.[21] *In situ* replacement by galvanic exchange has been effectively utilized to synthesize metal nanoparticles in a homogeneous phase.[12,21–23] Herein, we designed a heterogeneous catalyst by performing a replacement reaction, because *in situ* replacement is one of the exemplary methods in the synthesis of NPs. Through it, researchers can produce different fully reduced metal NPs with a specific atom at different times by maintaining the same number of metal precursors.[12,24]

One of the limiting factors associated with AuNPs is mobility and sintering at higher temperatures due to thermal instability. Thermal stability of catalysts is of crucial importance to some industrially generated high-temperature reactions such as hydrocracking, partial oxidation, and complete combustion.[25] Hence, an initial dual templating strategy of metal nanoparticles

was performed. However, to evaluate the activity of this catalyst in oxidation–reduction reactions, reduction of 4-nitrophenol, oxidation of rhodamine B (RhB), and oxidation of styrene were used as model reactions. 4-Nitrophenol and RhB are two of the prevalent pollutants commonly generated through industrial activities such as textiles, pharmaceuticals, cosmetics, dyeing, food additives, plastics, leather, printing, and other associated industries.[26,27] The degradation of 4-nitrophenol and RhB was observed at λ 400 and 554 nm, respectively, with time-resolved UV-vis spectroscopy.[28]

Over the years, studies have been repeatedly carried out on selective oxidation of styrene to styrene oxide, benzaldehyde, phenylacetaldehyde, acetophenone, and benzoic acid.[29–31] Phenylacetaldehyde and benzaldehyde have their applications in the synthesis of bulk chemicals, agricultural and fine chemical products, as chemical intermediates in the manufacturing of perfumes, pharmaceuticals, and dyes, and also, monitoring of insect control due to their aroma.[30,32] Reaction conditions and catalyst type have been reported to be the determinant of the product formation.[33] Therefore, previous reports, such as reaction temperature,[31] solvent type,[30] oxidant,[34] and catalyst amount[30] were selected as conventional reaction conditions. Hence with the result obtained, the selectivity of our catalysts was towards benzaldehyde, and phenylacetaldehyde only, as shown in Scheme 2, without unwanted products.

2. Experimental section

2.1. Chemicals and materials

Amine-terminated generation 4 PAMAM dendrimers (10 wt 5% in methanol), tetraethyl orthosilicate (TEOS) (99%), [HAuCl$_4$]·3H$_2$O (99.9%), 4-nitrophenol ($\geq$99.5%), rhodamine B ($\geq$99.90%), styrene ($\geq$99%), TBHP (70% in water), styrene oxide ($\geq$97%), 2-phenylacetaldehyde ($\geq$98%), benzaldehyde ($\geq$99%),

Scheme 2 Illustrative representation of the products formed from styrene oxidation.

dichloromethane (DCM) ($\geq$99.8%), acetonitrile ($\geq$99.9%), phosphate buffer (pH $\sim$ 7.87) with K_2HPO_4 (98%), hydrogen peroxide (H_2O_2) 30%, HCl (32%), sodium carbonate (Na_2CO_3) (90%) and $CuSO_4 \cdot 5H_2O$ were all acquired from Sigma-Aldrich. NaOH (99.9%), $KMnO_4$ (99.4%), and sodium bicarbonate ($NaHCO_3$) (99.60%) were obtained from Promack Chemicals. Perchloric acid ($HClO_4$) (70.0%), and $NaBH_4$ ($\geq$98.0%) were acquired from Fluka. All chemicals were used as obtained. All experimental analyses were performed using 18.2 MΩ cm Milli-Q water.

2.2. Synthesis of SiO$_2$ spheres

The silica spheres were prepared following a previous report with slight modification.[3] The synthesis began by transferring generation 4-NH_2 dendrimer (10 wt% in MeOH, 0.18 g, 1.28 $\times$ 10^{-6} M) into a round-bottom, two necked flask, for the removal of methanol *in vacuo*. Phosphate buffer, 60 mM was used to dissolve the dendrimer and diluted with degassed Milli-Q water to make a total volume of 8 mL and 0.16 mM. This was completed by a dropwise addition of silicic acid (5 mL) prepared by hydrolyzing TEOS in 1 mM HCl. The precipitate formed was centrifuged for 20 min at 3500 rpm. Finally, this was rinsed with degassed Milli-Q water before overnight drying at 70 $^\circ$C *in vacuo*.

2.3. Synthesis of Cu$_n$@SiO$_2$NPs with G4-PAMAM-NH$_2$ dendrimer as a stabilizer

In carrying out the synthesis, a procedure reported in the literature was adapted.[3] In summary, aqueous $CuSO_4$ solution made in a ratio of 16:1 of G4-PAMAM-NH2 dendrimer (40 μL, 0.1 M, 4.0 μmol) was pipetted to the preformed dendrimer in 60 mM phosphate buffer solution with consecutive addition of degassed Milli-Q deionized H_2O for a total volume of 8 mL. G4-PAMAM-NH_2/Cu^{2+} was stirred for 1 hr under an inert atmosphere to obtain thorough complexation at a fixed pH of 7.5. This was followed by a total reduction of the Cu^{2+} ions in solution through 10 molar excess of $NaBH_4$ (400 μL, 0.1 M, 0.5 μmol) for CuDEN formation. After that, preformed silicic acid was added slowly to the CuDENs, while stirring continuously under an inert atmosphere for 15 min. This leads to silica precipitation, which was collected by centrifuging the precipitate and drying overnight at 70 $^\circ$C. Finally, calcination was done for 3 h at 500 $^\circ$C using a 1 $^\circ$C min^{-1} heating rate to remove the template.

2.4. Preparation of Au$_n$@SiO$_2$NPs by *in situ* replacement

This was obtained using the stepwise description of Zhao and Crooks.[22] To start with, fine powder of Cu$_n$@SiO$_2$ obtained after calcination in the air was suspended in Milli Q water, stirred into slurry formation. This was reduced appropriately due to the possibility of oxidation since calcination was not carried out under

an inert environment. The pH of the obtained slurry was adjusted to 3.2 from 7.5 using 0.1 M $HClO_4$ before the addition of $HAuCl_4$ (40 μL, 0.1 M, 4.0 μmol). The addition of $HAuCl_4$ resulted in the color change from a brownish color to a light purple coloration. However, it was stirred for about 30 min at 25 $^\circ$C to ensure proper and complete replacement. The slurry was then centrifuged for 20 min at 3500 rpm, and the separated supernatant was dried *in vacuo* at 70 $^\circ$C to obtain powdered Au$_n$@SiO$_2$NPs.

2.5. Characterization of the catalyst

All spectrophotometric analyses obtained for monitoring the absorbance were carried out on a Shimadzu UV-1800 in 3 mL quartz cuvettes. The internal structure of the images was obtained by high-resolution transmission electron microscopy (HR-TEM), which was carried out using a JEOL JEM-2100F electron microscope of 200 kV voltage accelerator. This was done by suspending the fine powder of Cu$_n$@SiO$_2$NPs and Au$_n$@SiO$_2$NPs in water ultrasonically. A few drops of Cu$_n$@SiO$_2$NPs and Au$_n$@SiO$_2$NPs were placed upon Ni and Cu grids, respectively, and then set up for image capturing. Nitrogen sorption analyses of the samples were performed using a Micromeritics ASAP 2460 instrument. The samples were degassed at 90 $^\circ$C under nitrogen gas overnight. These samples were left to cool under vacuum to make their surfaces and pores available for probing. The data obtained were computed by the Brunauer–Emmett–Teller (BET) method to determine the samples' surface area, while the pore size distribution was calculated using the Barrett–Joyner–Halenda (BJH) method. A SDT Q600 thermogravimetric analyzer (TA Instrument) was used to determine the thermal stability of the samples between 0 and 1000 $^\circ$C at 10 $^\circ$C min^{-1} heating rate. A Shimadzu IRAffinity-1 was used to conduct the FTIR analysis. Powder X-ray diffraction analysis was executed with a Rigaku SmartLab at the 2θ range from 5° to 80° angle with Cu Kα radiation (λ = 1.54056 Å). All pH adjustments were conducted using an ORION model 520A pH meter with a Schott pH electrode blueline 25.

2.6. Catalytic reactions

A Shimadzu UV-1800 spectrophotometer was used to monitor the decrease in absorbance with the aid of quartz cuvettes (3 mL). The reduction was monitored at room temperature from λ 600 nm to λ 200 nm at an intermission of 3 min and 1 min, respectively, for both Cu$_n$@SiO$_2$NPs and Au$_n$@SiO$_2$NPs. Nitrophenol (4-NP; 0.2 μmol) was dissolved in 0.1 M NaOH to form a stock solution. A freshly made $NaBH_4$ solution (0.1 M, 0.32 mM) was added to a portion of 4-NP alongside different aliquots of Cu$_n$@SiO$_2$NPs and Au$_n$@SiO$_2$NPs. UV-vis measurement was then performed to monitor the time-resolved absorbance at each degradation step consecutively.

The oxidation of RhB was also investigated using a UV-vis spectrophotometer. An aqueous mixture of RhB (0.1 M) was prepared, and the concentration of the oxidant was determined through titration using potassium permanganate. The reaction was performed by first varying the amount of $Au_n@SiO_2NPs$ within the range of 0.3–0.7 mg, while the amount of substrate and oxidant remained constant in the presence of a freshly prepared carbonate buffer. The procedure was then repeated by varying the amount of substrate and oxidant at different times, while other parameters also remained constant. Adsorption of the substrate on the catalyst surface was carried out between 0.012 mM and 0.020 mM, while analysis of the oxidant adsorption on the catalyst was between 24 mM and 32 mM. A stable buffer (sodium carbonate and sodium hydrogen carbonate) medium of 7.5 pH was ensured throughout the process.[35] All verification was done with 3 mL quartz cuvettes.

Catalytic oxidation of styrene was performed with the use of a carousel TM multi-reactor (Radley Discovery Technologies) fitted to a reflux condenser. $Au_n@SiO_2NPs$ (0.1 g), 4.7 mmol (300 μL) of decane as an internal standard, 2 mmol (214 μL) styrene, and 3 mmol (415.2 μL) of TBHP were all pipetted into a 50 mL vial containing 10 mL acetonitrile (solvent). This was stirred at 450 rpm/80 °C. Samples for analysis were taken repeatedly at an interval of 1 h, for 6 h. Analyses of the products were performed using a Shimadzu GC-2010 Plus fitted with a flame ionization detector (FID) and a Restek-800-356-1688 capillary column (30 m × 0.25 mm × 0.25 μmol of film thickness). The injection port was set at 250 °C, while the FID temperature remained at 300 °C. The column temperature was regulated to 300 °C and the carrier gas was nitrogen gas.

3. Results and discussion

3.1. TEM Characterization of silica spheres, $Cu_n@SiO_2NPs$ and $Au_n@SiO_2NPs$

The morphological appearance of the silica spheres prepared in a 60 mM phosphate buffer solution is presented in Fig. 1a. It has been reported that parameters such as pH, temperature, and alkalinity have a remarkable effect on structural materials like silica.[36] Hence, the synthesis of the silica spheres under ambient temperature and at a pH of 7.87 brings about the spherical structure of the silica. This permits the ease of NP encapsulation. The particle size obtained (283.3 nm) is comparable to that which has been described under similar conditions.[3]

The TEM images presented in Fig. 1b and c revealed the internal morphology of both $Cu_n@SiO_2NPs$ and $Au_n@SiO_2NPs$ prepared by the templating method and displacement method, respectively. The histographical plot obtained for $Cu_n@SiO_2NPs$ revealed the particle size to be 3.7 ± 0.7 nm, which is an indication of narrowly dispersed NPs. The image obtained for $Au_n@SiO_2NPs$ revealed that the spherical structure of the silica framework was still preserved after a replacement had taken place. This also shows the successful encapsulation of the particles with an increase in the size distribution to 10.2 ± 3.7 nm. The notable increase could be as a result of calcination temperature at 500 °C for 3 h and decomposition of the organic dendrimer stabilizers that were present before calcination. Calcination has been reported to be responsible for a change in particle size[25] as a result of gradual growth in the number of atoms.[37] But it is interesting to note that this increase in $Au_n@SiO_2NP$ particle size did not hamper the catalyst effectiveness. The EDX analysis shown in Fig. S1 (ESI†) is evidence for the successful replacement of $Cu_n@SiO_2NPs$ with $Au_n@SiO_2NPs$.

3.2. FTIR measurement of silica sphere before and after calcination

To ascertain the bonding between the organic dendrimer and the silica sphere, the FTIR analysis was carried out within 500–4000 cm^{-1} vibration frequency. From Fig. 2, we observed weak C–N stretching/N–H bending vibrations on the uncalcined silica sphere. This can be ascribed to amide and amine groups at ν 1641 and 1551 cm^{-1}, respectively. Besides, dendrimer interaction with the silica sphere was also confirmed.[38] This observed interaction was only found in the silica sphere before calcination. After calcination at 500 °C, organic dendrimer decomposition had taken place. However, the appearance of
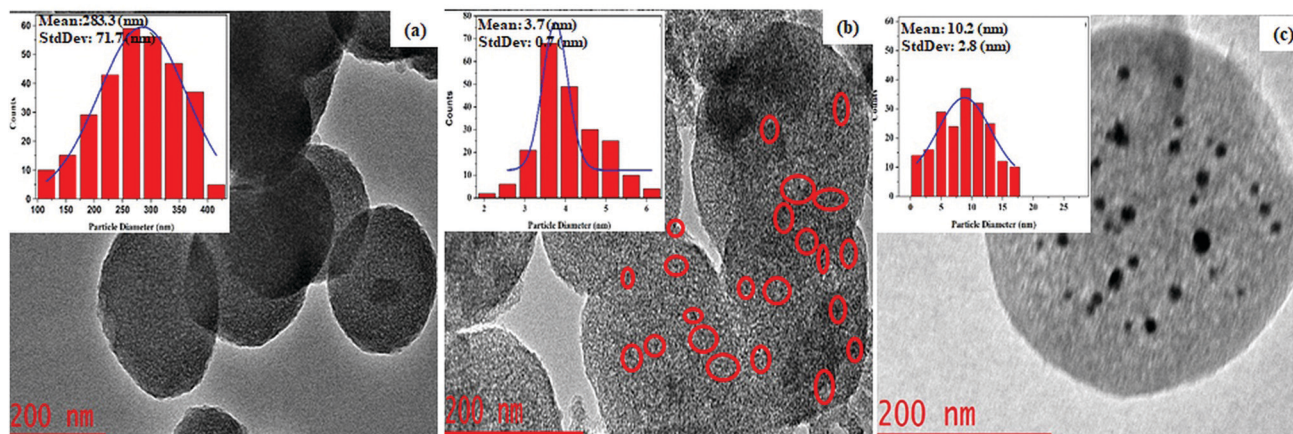

Fig. 1 The TEM images and histographical plots of (a) G4-PAMAM-NH$_2$ templated silica sphere (G4-PAMAM-NH$_2$-SiO$_2$) (b) Cu$_n$@SiO$_2$NPs and (c) Au$_n$@SiO$_2$NPs.
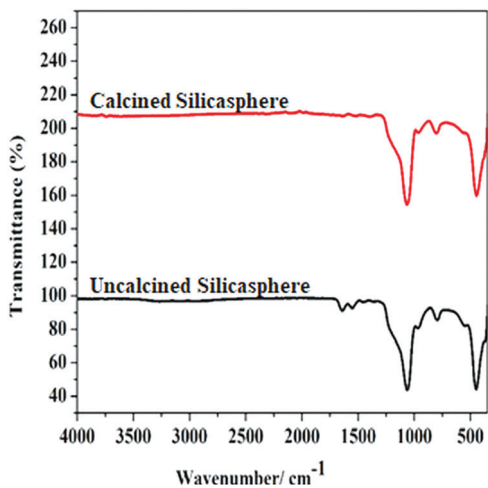
Fig. 2   FTIR analysis of dendrimer and silica sphere interaction.

bands at ν 1068, 790, and 452 cm^{-1} can be ascribed to the Si–O–Si stretching band.[36] The strong absorption at ν 969 cm^{-1} depicts Si–OH, which indicates that the silica spheres were free from moisture.[39]

3.3.   PXRD characterization

The PXRD characteristic patterns obtained for the catalysts are shown in Fig. 3. The peaks for Cu$_n$@SiO$_2$NPs and Au$_n$@SiO$_2$NPs displayed in Fig. 3a were indexed according to JCPDS number (89-2838)[40,41] and (04-0784),[42] respectively. The diffractogram of Cu at $2\theta = 34.3°$ can be ascribed to the 110 phase. The other peaks that were also observed at 39.4° and 57.8° were as a result of the oxidation of CuNPs[43–45] as the sample got exposed to air prior to analysis. These aligned with the JCPDS number 05-661. Moreover, four major characteristic peaks associated with Au at $2\theta = 38.1°$, 44.4°, 64.5°, and 77.6° were ascribed to (111), (200), (220), and (311) diffraction planes of the face-centered-cube (fcc). These characteristic peaks specific to metallic Au have been previously reported.[42] The diffraction peak around $2\theta = 23°$ specific to all the measurements in Fig. 3a and b is ascribed to amorphous silica.[46]

3.4.   Brunauer–Emmett–Teller nitrogen sorption analysis

The nitrogen adsorption–desorption isotherm capacity measurement of the surface area and pore structure of the samples that were taken are shown in Fig. 4a–d. With an exception of Cu$_n$@SiO$_2$ before calcination, all the hysteresis loops appeared in the range of 0.55–0.82P/P_0 with high surface areas. The isotherm curves of this form of hysteresis loop are particular to the type IV adsorption isotherm, which is a unique property of uniform mesopore distribution.[18,47] However, Cu$_n$@SiO$_2$ before calcination also possesses a type IV H3 hysteresis loop with no limit to adsorption even at high P/P_0 in between 0.8 and 1.0 including the desorption closure.[48] Moreover, the presence of a small hysteresis loop is an indication that the material possesses the characteristic porosity of which its surface area is 221.16 m^2 g^{-1}. This surface area drastically increased after calcination to 744.04 m^2 g^{-1} due to dendrimer removal at 500 °C.[46] Also, an increase in trend from 0.02731 cm^3 g^{-1} to 0.07150 cm^3 g^{-1} was seen in pore volume, while the surface area of the calcined Cu$_n$@SiO$_2$ is higher than the surface area of the calcined silica sphere. We believe this enlarged surface area might be caused by the increase in the adsorption sites on the surface of the calcined Cu$_n$@SiO$_2$ after the removal of the organic dendrimer during the calcination process. The surface area data, pore-volume, and pore size distribution obtained are outlined in Table 1.

3.5.   Thermogravimetric Analysis (TGA)

The thermal stability of the samples measured over time concerning the temperature change is presented in Fig. 5. The thermal profile obtained for both the silica sphere and Cu$_n$@SiO$_2$ in Fig. 5a and b respectively exhibit three different decomposition stages. The first degradation below 170 °C is due to the presence of adsorbed moisture, while the subsequent loss at 495 °C can be attributed to the decomposition of residues of the organic dendrimer.[49,50] The final step above 495 °C is ascribed to decomposition due to silanol condensation that formed oxides on the surface of the materials.[51–53] Breaking of siloxane bonds ($\equiv$Si–O–Si$\equiv$) can occur in
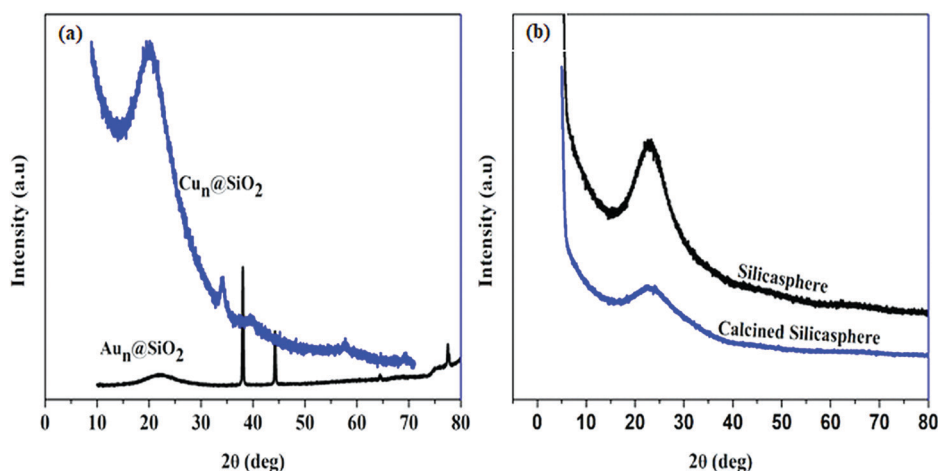

Fig. 3   PXRD patterns of (a) Cu$_n$@SiO$_2$ and Au$_n$@SiO$_2$ and (b) calcined and uncalcined silica spheres.
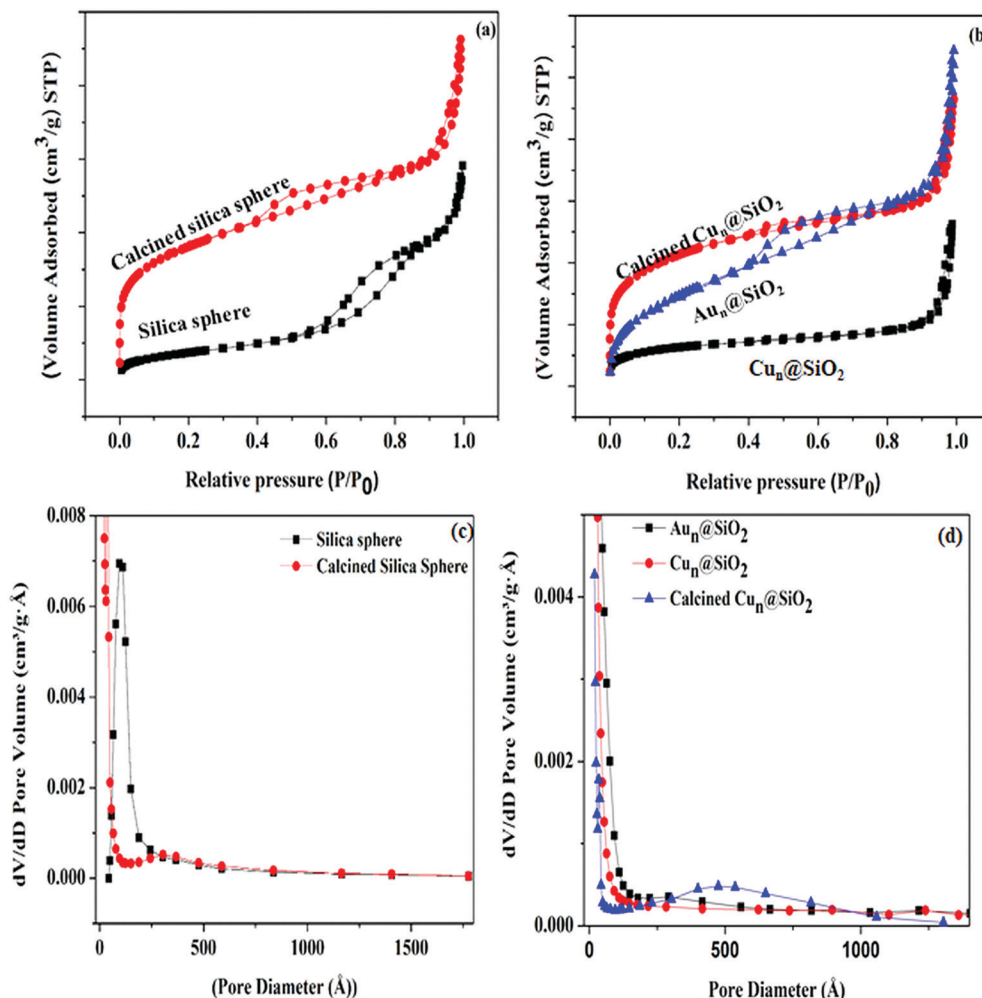
Fig. 4 N$_2$ adsorption–desorption isotherms of (a) silica sphere before and after calcination, and (b) Cu$_n$@SiO$_2$ before and after calcination, and Au$_n$@SiO$_2$. Pore distribution patterns of (c) silica sphere before and after calcination, and (d) Cu$_n$@SiO$_2$ before and after calcination, and Au$_n$@SiO$_2$.

Table 1 Surface area data and pore structure parameters of silica sphere, Cu$_n$@SiO$_2$ before and after calcination, and Au$_n$@SiO$_2$

All samples	BET surface area (m^2 g^{-1})	BJH pore volume (cm^3 g^{-1})	BJH pore diameter (nm)
Silica sphere	136.69	0.40829	11.945
Calcined silica sphere	632.55	0.07110	6.3257
Cu$_n$@SiO$_2$	221.16	0.02731	3.6261
Calcined Cu$_n$@SiO$_2$	744.04	0.07150	3.8441
Au$_n$@SiO$_2$	563.36	0.83954	5.9610

amorphous silica to form soluble silanols ($\equiv$Si–OH) through hydrolysis.[53] This is displayed in the FTIR spectra shown earlier. The Au$_n$@SiO$_2$ appeared to have two decomposition steps between 120 °C and 620 °C after which stability occurred, as shown in Fig. 5c. Based on the thermogram, the first thermal occurrence is as a result of adsorbed moisture loss and the second decomposition event occurred due to the emergence of the SiO$_2$ + Si reaction forming volatile 2SiO on the silica framework.[54]

3.5.1. Catalytic evaluation of the synthesized Cu$_n$@SiO$_2$ and Au$_n$@SiO$_2$ on 4-nitrophenol reduction. The reduction of 4-nitrophenol using NaBH$_4$ is a model reaction for investigating catalytically active metal nanoparticles.[55] Catalytic investigation of

Cu$_n$@SiO$_2$ and Au$_n$@SiO$_2$ on the reduction of 4-nitrophenol revealed good performance. An aqueous yellow solution of 4-nitrophenol displayed a maximum absorption peak at λ_{max} 400 nm. The addition of the catalyst and protonation of the reaction medium by NaBH$_4$ caused a change in coloration from yellow to a colorless solution. The simultaneous reduction also followed this as new absorbance intensity at λ 300 nm emerged. This is an indication of the reduction of 4-nitrophenol to form 4-aminophenol.[25] Fig. 6a and b revealed the time-dependent decline in the UV-vis absorption spectra obtained for the catalytic reduction of Cu$_n$@SiO$_2$ and Au$_n$@SiO$_2$, respectively. Reaction with Au$_n$@SiO$_2$ was completed within 10 min, while it took 30 min for
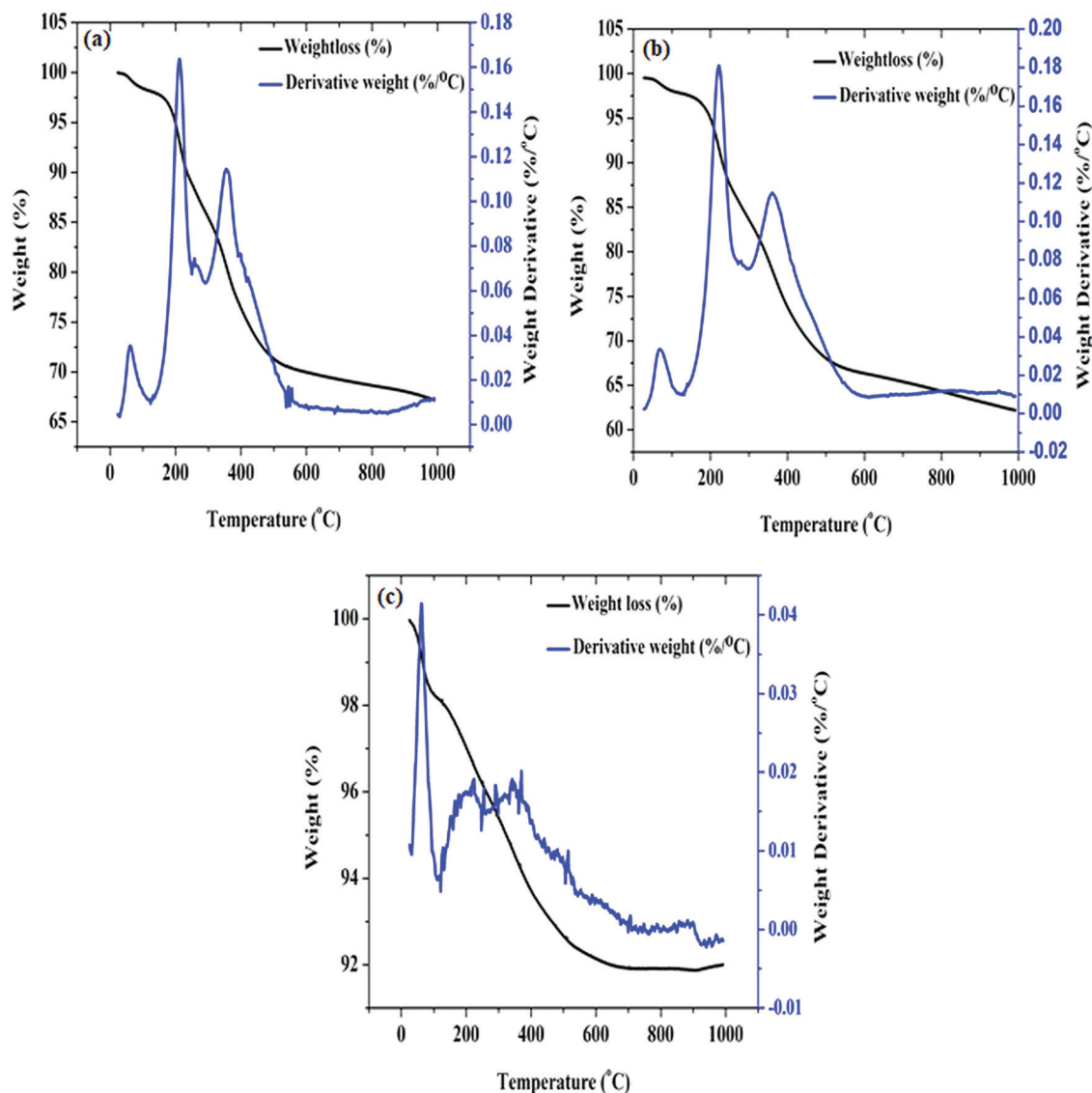
Fig. 5 Thermogravimetric analysis of (a) silica spheres, (b) $Cu_n@SiO_2$, and (c) $Au_n@SiO_2$.

reduction to be achieved with $Cu_n@SiO_2$. Considering the time taken for the reaction to be completed by the two catalysts, it is evident that $Au_n@SiO_2$ is more effective. The non-linear regression with respect to time presented in Fig. 6c and d aligned with a pseudo-first order reaction. However, the reduction reaction conducted in the absence of both $Cu_n@SiO_2$ and $Au_n@SiO_2$ catalysts (result not shown) displayed no change in the peak intensity. This confirmed that the reduction was catalytically enhanced.

3.5.2. Catalytic investigation on oxidation of RhB. Oxidation of RhB carried out in the presence of H_2O_2 can also be utilized as a model reaction to access the catalytic influence of the metal nanoparticles.[56] With the establishment of $Au_n@SiO_2$ as an effective catalyst in 4-nitrophenol reduction, the UV-vis spectrum of RhB oxidation obtained at an interval of 3 min for its degradation using $Au_n@SiO_2$ is presented in Fig. 7a. The catalytic decomposition was observed within 30 min at each degradation process using different amounts of the catalyst as

shown in Fig. 7b. This revealed that an increase in catalytic performance is directly proportional to an increase in catalyst amount. Considering the mathematical expression of the kinetic pseudo-first-order used in eqn (1),[57] A_0, and A_t represent an initial concentration of RhB and concentration at time t, respectively. A_∞ is the final concentration of RhB, while k_{obs} denotes the observed rate constant.

$$-\ln\frac{A_t - A_\infty}{A_0 - A_\infty} = k_{obs} \times t \qquad (1)$$

The catalytic reaction order conformed to a pseudo-first-order reaction. The plot is shown in Fig. S2 (ESI†). Also, a carbonate buffer mixture with a pH of 7.5 containing Na_2CO_3 and $NaHCO_3$ added ensured H_2O_2 stability and enhanced adsorption all through the reaction.[33] This was because the force due to repulsion between the catalyst and the dye was limited.[58] The observed rate constant *versus*
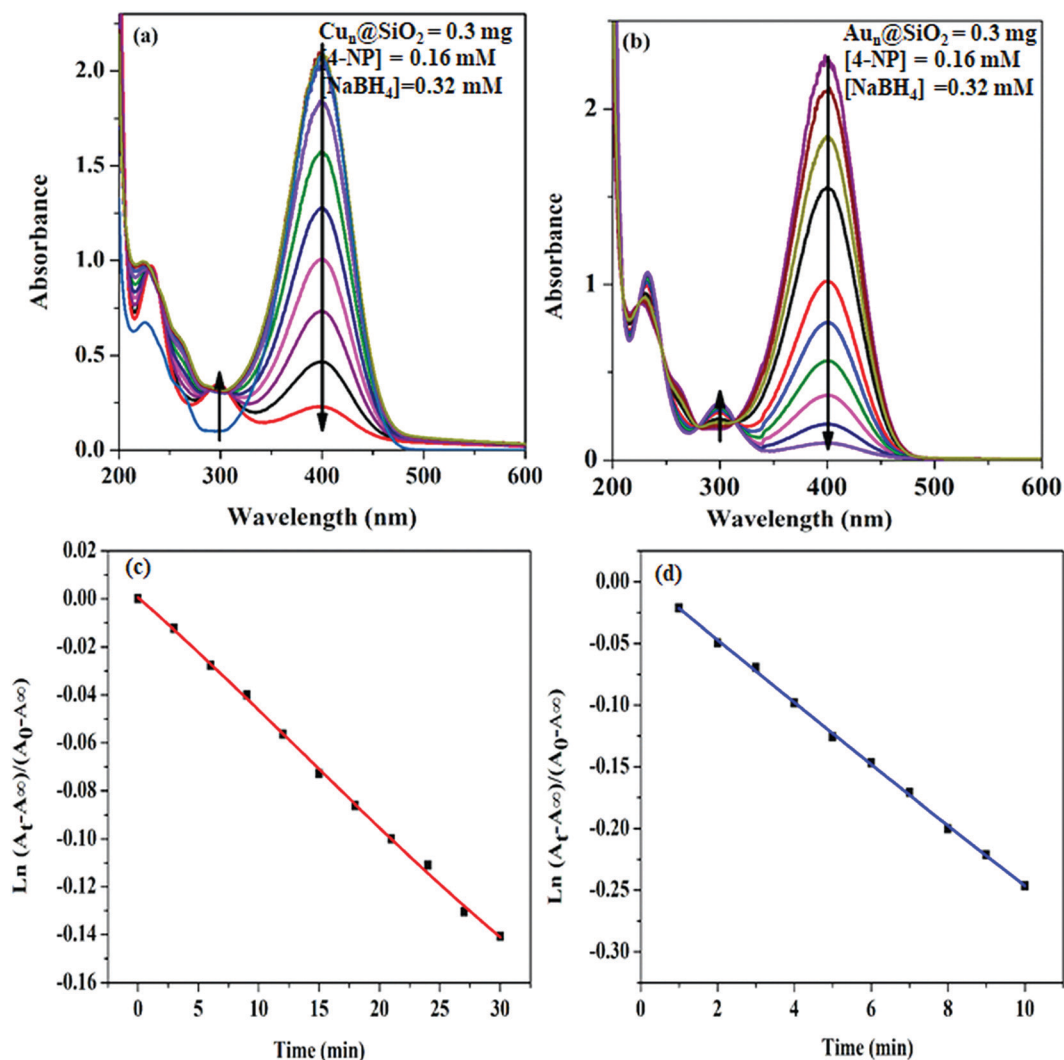
Fig. 6 UV-vis spectra showing the degradation of 4-nitrophenol using (a) Cu_n@SiO_2 and (b) Au_n@SiO_2; non-linear regression against time with (c) Cu_n@SiO_2 and (d) Au_n@SiO_2.
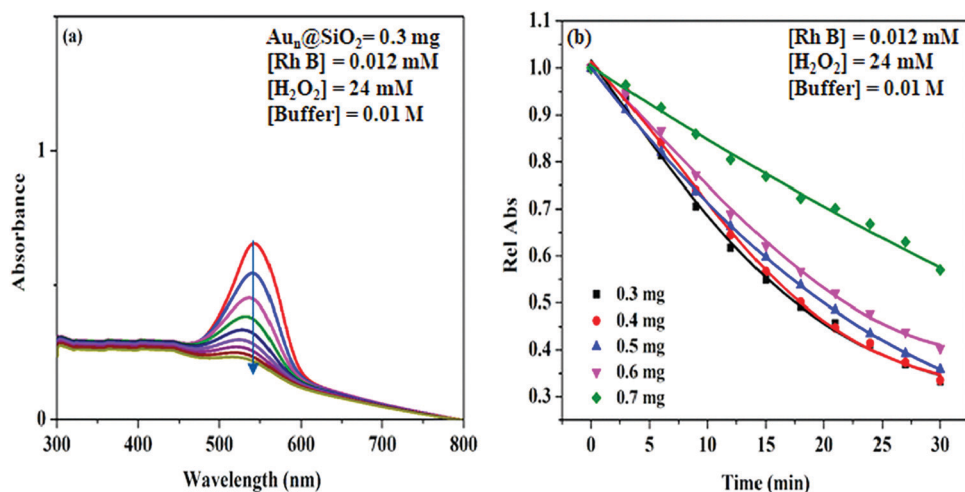

Fig. 7 (a) UV-vis spectrum of RhB oxidation by using Au_n@SiO_2, and (b) non-linear fits of data.
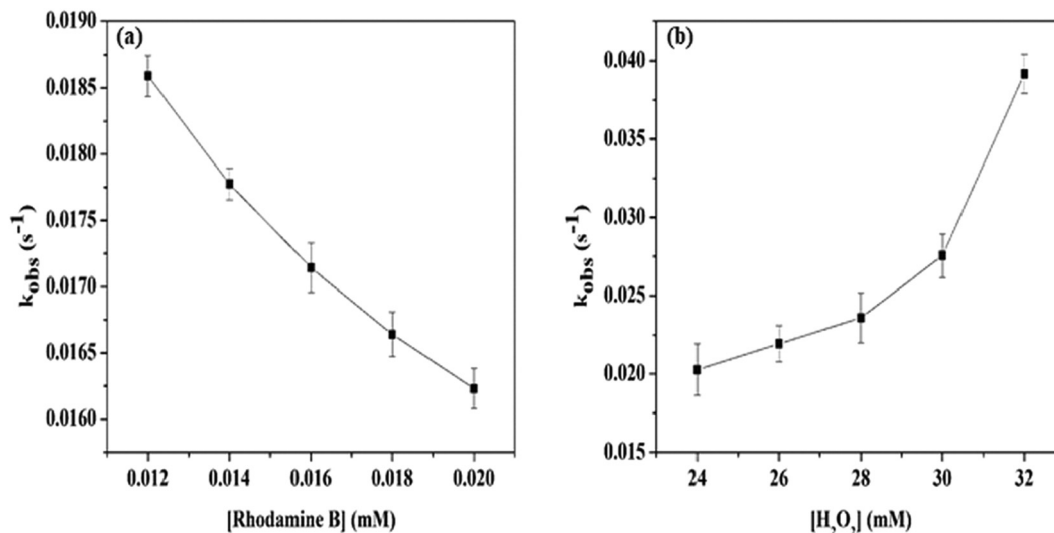
Fig. 8 Concentration variations of (a) RhB and (b) H_2O_2.

concentration of RhB adsorption on the catalyst surface in Fig. 8a, decreased with an increase in substrate amount due to dye saturation on the catalyst surface. This is an indication that the reaction rate is a function of catalyst availability. In Fig. 8b, the analysis of H_2O_2 adsorption shows a concurrent increase with respect to the oxidant due to an increase in the supply of oxygen from H_2O_2, thereby hastening the decomposition of the substrate.

3.5.3. Catalytic evaluation of Au$_n$@SiO$_2$ in the oxidation of styrene to benzaldehyde and phenylacetaldehyde.

The catalytic evaluation of the as-synthesized Au$_n$@SiO$_2$ catalyst was also carried out on the oxidation of styrene in the liquid phase using TBHP as an oxidant. At the same time, acetonitrile served as the solvent at 80 °C. Heterogeneous catalytic oxidation of styrene gave selectivity towards phenylacetaldehyde (PA) and benzaldehyde

(BzA) as the primary products. The obtained result is presented in Fig. 9a. A record of progressive reaction and a proportional increase in conversion as time proceeds with maximum styrene conversion of 54.3% is obtained. Conversion of styrene is expressed as the percentage converted into a product to the total percentage initially present in the reaction mixture. The reaction, which was found to be selective towards both benzaldehyde and phenylacetaldehyde produced a higher selectivity of 64.4% towards phenylacetaldehyde and 35.6% for benzaldehyde. Moreover, the reaction mixture did not display the presence of other products from the analysis, especially acid formation that results from co-oxidation of benzaldehyde.[59] The selectivity of the catalyst is suspected to be enhanced by the surface electronic distribution, surface morphology, and particle size of Au.[37,60] It has been reported that the electronic nature of Au catalyst sites
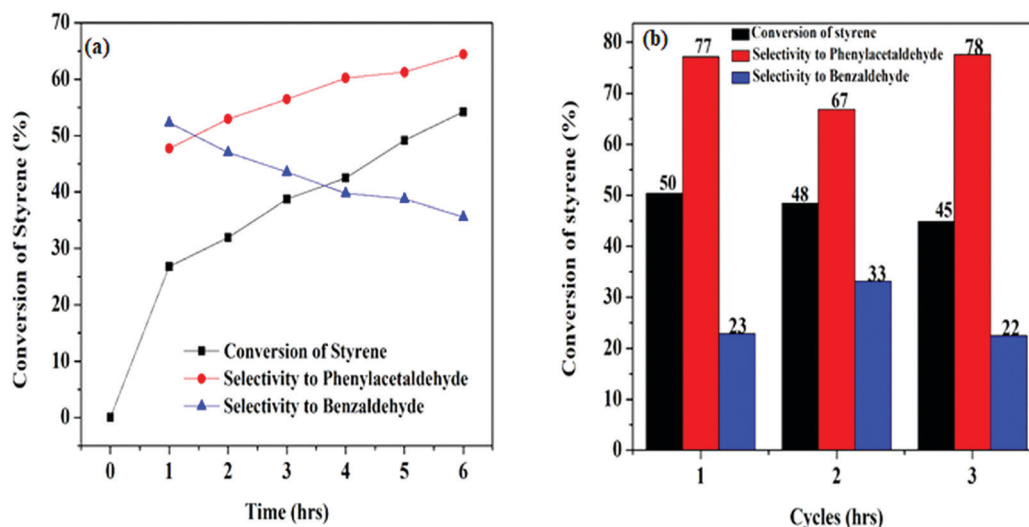

Fig. 9 (a) Plots revealing conversion and selectivity of Au$_n$@SiO$_2$ at 80 °C: 0.1 g catalyst, 0.59 wt% metal loading, 214 μL (2 mmol) styrene, 415.2 μL (3 mmol) TBHP, and 6 h and (b) catalyst recyclability.

Table 2 Oxidation comparison with other previous reports on Au-based catalysts

| Catalysts | Au (wt%) | Time (h) | Temp. (°C) | Oxidant | TOF (h^{-1}) | Conv. (%) | Selectivity (%) | | | | Ref. |
							PA	BzA	SO	Others	
Ti–Au-s	1.3	15	70	TBHP	—	41.0	—	61.0	39.0	—	63
Ti–Au-w	1.8	15	70	TBHP	—	23.0	—	67.0	33.0	—	63
Au/SrO	0.6	24	80	TBHP	—	21.4	26.0	11.7	44.8	17.4	65
Au/MgO (HDP)	4.1	24	80	TBHP	—	44.6	16.8	10.8	54.3	18.1	65
1Au$_{25}$/AC	1.0	16	80	TBHP	—	35.3	—	—	4.3	—	64
1Au$_{25}$/PGO	1.0	16	80	TBHP	—	44.8	—	—	5.6	—	64
1Au$_{25}$/SiO$_2$-300	1.0	16	80	TBHP	—	46.9	—	—	14.7	—	64
Au/BaTNT	1.0	15	80	TBHP	182	46.8	4.8	18.9	70.9	5.4	66
Au/BaTNT	0.5	15	80	TBHP	273	31.0	3.4	14.0	75.8	6.8	66
Au$_{25}$/SiO$_2$	2.0	24	82	TBHP	103 $\pm$ 10	15.1	—	6.6	93.4	—	25
Au$_n$@SiO$_2$	0.59	6	80	TBHP	306	54.3	64.4	35.6	—	—	This work

Reaction conditions: 0.1 g of catalyst, 0.59 wt% metal loading, 214 μL (2 mmol) of styrene, 415.2 μL (3 mmol) of TBHP, temperature 80 °C, and 6 h; conversion = (converted styrene)/(initial amount of styrene) × 100.

has a tuning effect on their catalytic activity and selectivity.[61] Hence the structure of Au$_n$@SiO$_2$ permits a rearrangement of hydrogen through ring-opening, thereby giving rise to phenylacetaldehyde,[30] while benzaldehyde formation occurred through oxidative cleavage.[62]

An important parameter of heterogeneity in catalysis is the ease of recoverability and recyclability from the reaction medium. This economic attribute makes them preferable over homogeneous catalysts. Au$_n$@SiO$_2$ was evaluated for its recyclability after recovering it from the reaction medium as shown in Fig. 9b. The catalyst displayed no severe deterioration of activity, and it is shown to be continuously selective towards both benzaldehyde and phenylacetaldehyde with stable higher selectivity to phenylacetaldehyde. In respect of the Au loading amount and the possibility of catalyst leaching into the reaction solution, inductively coupled plasma-optical emission spectroscopy (ICP-OES) measurements revealed the Au loading amount to be 0.59 wt%. It also showed that an insignificant amount of 0.03 mg L^{-1} of Au was present in the solution after the reaction. These reports, including the turnover frequency (TOF) of 306 h^{-1} are all indications that the Au NPs are well immobilized and encapsulated on the silica sphere.

The effect of air involvement on the mechanistic transformation of styrene to phenylacetaldehyde and benzaldehyde was considered since the reaction was performed in an open-air condition. The reaction carried out in the absence of TBHP oxidant showed that less than 0.5% conversion was recorded (graph not shown). From this result, it is evident that there was just a little and insignificant effect of oxygen on the reaction for the observed period of 6 h. However, when the reaction was verified with only the aqueous TBHP oxidant, we found only 8.2% conversion (Fig. S3, ESI†). This confirmed TBHP as the principal oxidant,[63] which provided a substantial oxidative environment for the reaction.[64]

A comparison of the catalytic activity of Au$_n$@SiO$_2$ on styrene oxidation was made with previously reported gold catalysts. As shown in Table 2, confirmation of this catalyst being in fair comparison in terms of TOF and conversion with other previously reported gold-based catalysts can be made because it has the highest TOF value and conversion percentage (%). The

reaction time was much shorter, and the Au loading amount was lower than every other catalyst. Although there was no selectivity towards styrene oxide (SO) using Au$_n$@SiO$_2$, which was seen in every other catalyst, an outstanding feature of this catalyst is its selectivity towards phenylacetaldehyde and benzaldehyde. We propose this may have originated from the encapsulation of Au in the silica sphere after direct replacement and change in particle size, pore size, and surface area.

4. Conclusion

The systematic protocol of the CuDEN templating approach enabled the encapsulation of small-sized CuNPs into the silica sphere as Cu$_n$@SiO$_2$. The *in situ* replacement by galvanic exchange controlled by the difference in the electrode potential was successfully achieved. Both the preliminary catalytic activity of Cu$_n$@SiO$_2$ and Au$_n$@SiO$_2$ on the reduction of 4-nitrophenol using NaBH$_4$ showed a distinctive pattern of a pseudo-first-order reaction. Au$_n$@SiO$_2$ possessed an improved catalytic performance and also revealed an efficient activity on oxidation of RhB using H$_2$O$_2$. This also aligned to a pseudo-first-order reaction. An increase in the concentration of RhB brought about a decrease in k_{obs} with a subsequent increase in k_{obs} as peroxide concentration increased.

Furthermore, concerning the reaction conditions, the catalyst also efficiently catalyzed the styrene oxidation with 54.3% conversion. This gives 35.6% and 64.4% selectivity towards benzaldehyde and phenylacetaldehyde, respectively. The yield is both selective and quantitative, while the stability of the catalyst was also retained after three consecutive cycles.

Conflicts of interest

The authors declare no competing financial interest.

Acknowledgements

References

1 X. Peng, Q. Pan and G. L. Rempel, *Chem. Soc. Rev.*, 2008, **37**, 1619.

2 P. Ncube, N. Bingwa, H. Baloyi and R. Meijboom, *Appl. Catal., A*, 2015, **495**, 63–71.

3 M. Nemanashi-Maumela, I. Nongwe, R. C. Motene, B. L. Davids and R. Meijboom, *Mol. Catal.*, 2017, **438**, 184–196.

4 M. Zhao and R. Crooks, *Angew. Chem., Int. Ed.*, 1999, **38**, 364–366.

5 R. M. Crooks, M. Zhao, L. I. Sun, V. Chechik and L. K. Yeung, *Acc. Chem. Res.*, 2001, **34**, 181–190.

6 H. Lang, R. May, B. Iversen and B. Chandler, *J. Am. Chem. Soc.*, 2003, **125**, 14832–14836.

7 R. W. J. Scott, O. M. Wilson and R. M. Crooks, *J. Phys. Chem. B*, 2005, **109**, 692–704.

8 Z. V. Feng, J. L. Lyon, J. S. Croley, R. M. Crooks, D. A. Vanden Bout and K. J. Stevenson, *J. Chem. Educ.*, 2009, **86**, 368–372.

9 V. S. Myers, M. G. Weir, E. V. Carino, D. F. Yancey, S. Pande and R. M. Crooks, *Chem. Sci.*, 2011, **2**, 1632.

10 M. Nemanashi and R. Meijboom, *J. Colloid Interface Sci.*, 2013, **389**, 260–267.

11 N. Bingwa and R. Meijboom, *J. Phys. Chem. C*, 2014, **118**, 19849–19858.

12 T. Cho, C. W. Yoon and J. Kim, *Langmuir*, 2018, **34**, 7436–7444.

13 G. Duan, Æ. C. Zhang, A. Li, Æ. X. Yang, Æ. L. Lu and Æ. X. Wang, *Nanoscale Res. Lett.*, 2008, **3**, 118–122.

14 K. Nakanishi, M. Tomita, Y. Masuda and K. Kato, *New J. Chem.*, 2015, 4070–4077.

15 M. Huang, L. Liu, S. Wang, H. Zhu, D. Wu, Z. Yu and S. Zhou, *Langmuir*, 2017, **33**, 519–526.

16 N. Qiao, X. Zhang, C. He, Y. Li, Z. Zhang, J. Cheng and Z. Hao, *Front. Environ. Sci. Eng.*, 2016, **10**, 458–466.

17 H. Zhang, J. Wu, L. Zhou, D. Zhang and L. Qi, *Langmuir*, 2007, **23**, 1107–1113.

18 C. Paper, Y. Pan and W. Cheng, *Adv. Mater. Res.*, 2013, **785–786**, 382–385.

19 J. Zhou, T. Yang, W. He, Z. Y. Pan and C. Z. Huang, *Nanoscale*, 2018, **10**, 12805–12812.

20 M. B. Gawande, A. Goswami, T. Asefa, X. Huang, R. Silva, X. Zou, R. Zboril and R. S. Varma, *Chem. Rev.*, 2016, **116**, 3722–3811.

21 S. Pande, M. G. Weir, B. A. Zaccheo and R. M. Crooks, *New J. Chem.*, 2011, **35**, 2054–2060.

22 M. Zhao and R. M. Crooks, *Chem. Mater.*, 1999, **11**, 3379–3385.

23 R. M. Anderson, D. F. Yancey, J. A. Loussaert and R. M. Crooks, *Langmuir*, 2014, **30**, 15009–15015.

24 M. S. Xaba, J. Noh and R. Meijboom, *Appl. Surf. Sci.*, 2019, **467–468**, 868–880.

25 V. Sudheeshkumar, A. Shivhare and R. W. J. Scott, *Catal.: Sci. Technol.*, 2017, **7**, 272–280.

26 J. Luo, Y. Gao, K. Tan, W. Wei and X. Liu, *Sustainable Chem. Eng.*, 2016, **4**, 3316–3326.

27 M. S. Tehrani and R. Zare-dorabei,, *RSC Adv.*, 2016, **6**, 27416–27425.

28 S. Wunder, F. Polzer, Y. Lu, Y. Mei and M. Ballauff, *J. Phys. Chem.*, 2010, **114**, 8814–8820.

29 J. Noh, R. Patala and R. Meijboom, *Appl. Catal., A*, 2016, **514**, 253–266.

30 N. Masunga, B. P. Doyle, E. Carleschi and R. Meijboom, *Appl. Catal., A*, 2018, **559**, 175–186.

31 T. A. G. Duarte, A. P. Carvalho and L. M. D. R. S. Martins, *Catal. Today*, 2020, **357**, 56–63.

32 C. Guo, Y. Zhang, L. Zhang, Y. Guo, N. Akram and J. Wang, *ACS Appl. Nano Mater.*, 2018, **1**, 5289–5296.

33 M. S. Xaba, J. Noh, K. Mokgadi and R. Meijboom, *Appl. Surf. Sci.*, 2018, **440**, 1130–1142.

34 V. Chaudhary, *Chin. J. Chem. Eng.*, 2018, **26**, 1300–1306.

35 B. Cuiping, X. Xianfeng, G. Wenqi, F. Dexin, X. Mo, G. Zhongxue and X. Nian, *Desalination*, 2011, **278**, 84–90.

36 N. H. Khdary, M. A. Ghanem, M. E. Abdesalam and M. M. Al-garadah, *J. Saudi Chem. Soc.*, 2018, **22**, 343–351.

37 Y. Zheng, X. Zhang and Y. Yao, *RSC Adv.*, 2015, **5**, 105747–105752.

38 H. Kavas, Z. Durmus and E. Tanrıverdi, *J. Alloys Compd.*, 2011, **509**, 5341–5348.

39 Y. S. Chaudhary, J. Ghatak, M. Bhatta and D. Khushalani, *J. Mater. Chem.*, 2006, **16**, 3619–3623.

40 Z. Zhang, S.-S. Wang, R. Song, T. Cao, L. Luo, X. Chen, Y. Gao, J. Lu, W.-X. Li and W. Huang, *Nat. Commun.*, 2017, **8**, 1–10.

41 M. Ahamed, H. A. Alhadlaq, M. A. Khan, P. Karuppiah and N. A. Al-Dhabi, *J. Nanomater.*, 2014, DOI: 10.1155/2014/637858.

42 W. Shen, Y. Qu, X. Pei, S. Li, S. You, J. Wang, Z. Zhang and J. Zhou, *J. Hazard. Mater.*, 2017, **321**, 299–306.

43 J. Li, T. Shi, C. Feng, Q. Liang, X. Yu, J. Fan, S. Cheng, G. Liao and Z. Tang, *Mater. Lett.*, 2018, **216**, 20–23.

44 A. Kumar, A. Saxena, A. De, R. Shankar and S. Mozumdar, *RSC Adv.*, 2013, **3**, 5015–5021.

45 A. S. Lanje, S. J. Sharma, R. B. Pode and R. S. Ningthoujam, *Adv. Appl. Sci. Res.*, 2010, **1**, 36–40.

46 Q. Yao, Z. Lu, Z. Zhang and Y. Lan, *Sci. Rep.*, 2014, **4**, 7597.

47 M. Thommes, K. Kaneko, A. V. Neimark, J. P. Olivier, F. Rodriguez-reinoso, J. Rouquerol and K. S. W. Sing, *IUPAC Technical Report*, 2015, **87**, 1051–1069.

48 M. Thommes, *Chem. Ing. Tech.*, 2010, **82**, 1059–1073.

49 O. Ozturk, T. J. Black, K. Perrine, K. Pizzolato, C. T. Williams, F. W. Parsons, J. S. Ratliff, J. Gao, C. J. Murphy, H. Xie, H. J. Ploehn and D. A. Chen, *Langmuir*, 2005, 3998–4006.

50 B. A. Howell, D. Fan and L. Rakesh, *J. Therm. Anal. Calorim.*, 2006, **85**, 17–20.

51 X. Guo, M. Lai, Y. Kong, W. Ding, Q. Yan and C. T. P. Au, *Langmuir*, 2004, **20**, 2879–2882.

52 M. C. Rogers, B. Adisa and D. A. Bruce, *Catal. Lett.*, 2004, **98**, 29–36.

53 G. Yang, D. Wibowo, J. Yun, L. Wang, A. P. J. Middelberg and C. Zhao, *Langmuir*, 2017, **33**, 5777–5785.

54 I. Ilkiv, K. Kotlyar, D. Amel, S. Lebedev and G. Cirlin, *Acta Phys. Pol.*, 2017, **132**, 366–368.

55 S. I. Park and H. Song, *ACS Omega*, 2019, **4**, 7874–7883.

56 H. Liang, S. Liu, H. Zhang, X. Wang and J. Wang, *RSC Adv.*, 2018, **8**, 13625–13634.

57 A. K. Ilunga, T. Khoza, E. Tjabadi and R. Meijboom, *ChemistrySelect*, 2017, **2**, 9803–9809.

58 A. K. Ilunga and R. Meijboom, *J. Mol. Catal. A: Chem.*, 2016, **411**, 48–60.

59 T. Jiang, G. Gao, C. Yang, Y. Mao, M. Fang and Q. Zhao, *J. Nanosci. Nanotechnol.*, 2020, **20**, 1670–1677.

60 R. Jain and C. S. Gopinath, *Dalton Trans.*, 2019, 4574–4581.

61 B. Liu, P. Wang, A. Lopes, L. Jin, W. Zhong, Y. Pei, S. L. Suib and J. He, *ACS Catal.*, 2017, **7**, 3483–3488.

62 A. Blanckenberg, G. Kotze, A. J. Swarts and R. Malgas-Enus, *J. Nanoparticle Res.*, 2018, **20**, 44.

63 M. Nemanashi and R. Meijboom, *Catal. Lett.*, 2013, **143**, 324–332.

64 J. Fang, J. Li, B. Zhang, X. Yuan, H. Asakura, T. Tanaka, K. Teramura, J. Xie and N. Yan, *Nanoscale*, 2015, **7**, 6325–6333.

65 A. S. Sharma, D. Shah and H. Kaur, *RSC Adv.*, 2015, **5**, 42935–42941.

66 D. Nepak and D. Srinivas, *Appl. Catal., A*, 2016, **523**, 61–72.